



Convection behind the Humidification of Titan's Stratosphere

P. Rannou¹, M. Coutelier¹, E. Rivière¹, S. Lebonnois², M. Rey¹, and L. Maltagliati³

¹ GSMA, Université de Reims Champagne-Ardenne, France UMR 7331, CNRS, Université de Reims Champagne-Ardenne, Campus Sciences Exactes et Naturelles, BP 1039, F-51100 Reims, France; pascal.rannou@univ-reims.fr

² Laboratoire de Météorologie Dynamique, IPSL, Sorbonne Université, Paris, France

³ Nature Astronomy, Springer Nature, 4 Crinan Street, London N1 9XW, UK

Received 2021 August 8; revised 2021 September 20; accepted 2021 September 20; published 2021 December 3

Abstract

On Titan, methane is responsible for the complex prebiotic chemistry, the global haze, most of the cloud cover, and the rainfall that models the landscape. Its sources are located in liquid reservoirs at and below the surface, and its sink is the photodissociation at high altitude. Titan's present and past climates strongly depend on the connection between the surface sources and the atmosphere upper layers. Despite its importance, very little information is available on this topic. In this work, we reanalyze two solar occultations made by Cassini before the northern spring equinox. We find a layer rich in methane at 165 km and at 70°S (mixing ratio $1.62\% \pm 0.1\%$) and a dryer background stratosphere (1.1%–1.2%). In the absence of local production, this reveals an intrusion of methane transported into the stratosphere by convective circulation. On the other hand, methane transport through the tropopause at a global scale appears quite inhibited. Leaking through the tropopause is an important bottleneck of Titan's methane cycle at all timescales. As such, it affects the long-term evolution of Titan's atmosphere and the exchange fluxes with the surface and subsurface reservoirs in a complex way. Global climate models accounting for cloud physics, thermodynamical feedbacks, and convection are needed to understand the methane cycle, and specifically the humidification of the stratosphere, at the present time, and its evolution under changing conditions at a geological timescale.

Unified Astronomy Thesaurus concepts: [Planetary atmospheres \(1244\)](#); [Planetary climates \(2184\)](#); [Atmospheric composition \(2120\)](#)

1. Introduction

There are details about Titan's methane cycle that remain unknown. The main methane reservoirs are in lakes, seas, and possibly the subsurface (Mastrogiuseppe et al. 2014). Efforts have been made to understand the main characteristics of the methane tropospheric cycle (Lora et al. 2015; Faulk et al. 2020), that is, the global fluxes in the troposphere and the surface and subsurface sources and sinks. Radio-occultation measurements were used along with arguments involving circulation, observed cloud cover, and wind measured by Huygens to state that, before the northern spring equinox in 2009, the troposphere was more humid in the southern hemisphere than in the northern hemisphere (Tokano 2014). This is a valuable, although quite loose, constraint. Using photometric observations collected in 2014, Lora & Ádámkóvics (2017) found with certainty a very humid north polar region and, consistent with Tokano (2014), but not in a significant way, a methane humidity increasing from the north (30°N–60°N) to the southern hemisphere (30°S to the equator). However, clear conclusions at a global scale could not be drawn due to uncertainties in methane retrievals. Retrieving methane abundance is extremely difficult because optical properties of the haze and the tropospheric mist are not well defined. Observations of scattered light at the limb or in nadir viewing do not allow the disentanglement of methane abundance and particles without ambiguity. Thermal infrared emission observed with the Composite InfraRed Spectrometer (CIRS/Cassini) allows the retrieval of the methane mixing ratio, but with a low spatial resolution and only in the stratosphere. This is enough to describe latitudinal variations, but not vertical profiles (Lellouch et al. 2014). In the low and middle stratosphere, they generally found methane abundances

lower than expected from Huygens (Niemann et al. 2010) with strong variations and high values above the tropics and the polar regions, possibly connected to the circulation. With the Ultraviolet Spectrometer UVIS/Cassini, Yelle et al. (2021) also found a low methane mixing ratio, around 1% at 950 km, around the homopause.

We reanalyzed two occultations made by the Visual Infrared Mapping Spectrometer (VIMS/Cassini) during the flybys T10 in 2006 January and T53 in 2009 April, previously published and analyzed (Maltagliati et al. 2015). These observations are performed before the equinoctial turnover in 2009, while the large-scale circulation has remained steady for a Titan season and a half ($\simeq 11$ terrestrial years) (Rannou et al. 2004; Lebonnois et al. 2012). We used the methane linelist published by Rey et al. (2018) that significantly improves the quality of the retrievals. Details about the model, the results, and comparisons with the previous analysis are discussed in the Appendix. Occultations probe extinction along tangential lines of sight at the limb and they easily allow us to separate methane and haze extinction. In the following, we discuss our retrieval for the methane mixing ratio.

2. Description of the Method

To proceed to the analysis, we calculate the haze and the gas properties in Titan's atmosphere following Rannou et al. (2018) and Coutelier et al. (2021). Since we deal with occultation data, only extinction properties are needed. Then, we built a simple model for computing tangential transmissions through an atmosphere, as observed with the occultation mode. The vertical grid of the model is adjusted to the number of data N_D . We then define as many layers as data points. We set the haze properties and the methane abundance at the lower

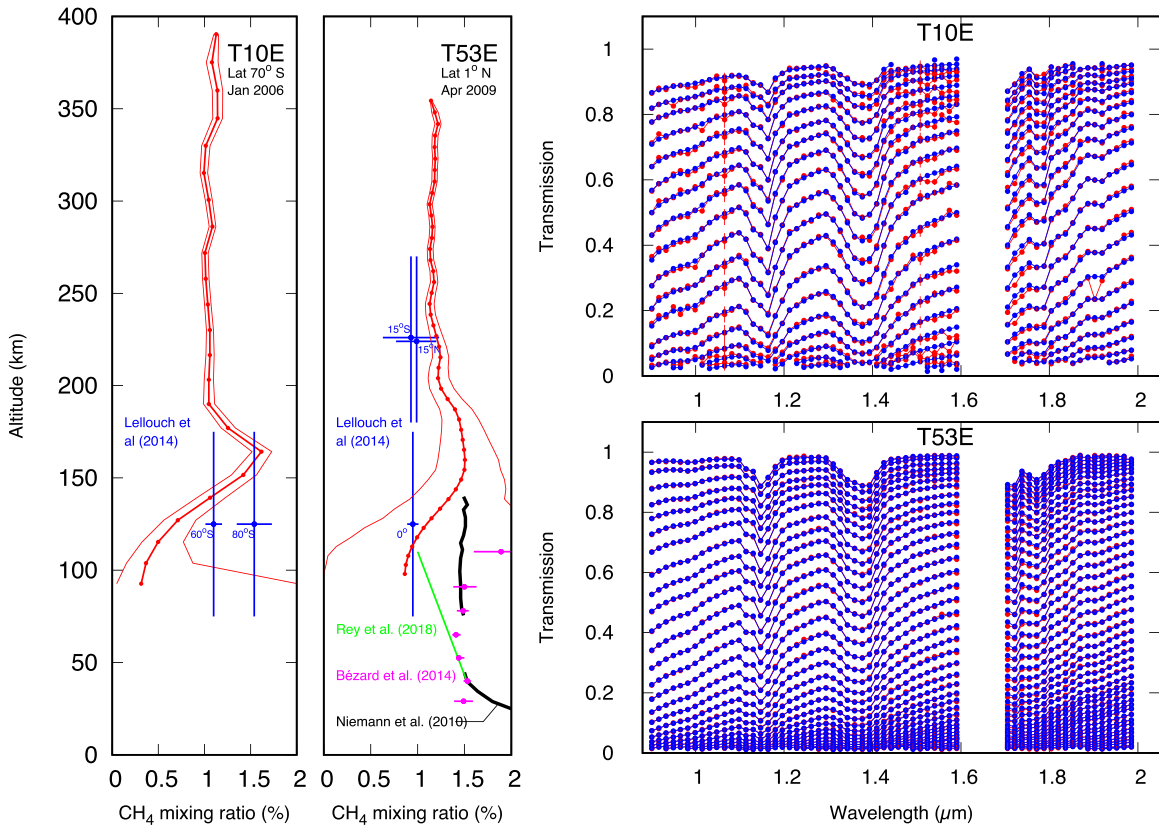


Figure 1. Left two panels: retrieved methane mixing ratio (red dots) and the related error envelope (red curves) with the two observation sets, between 0.88 and 2 μm . For observation T10, we also plot the retrieval made with the CIRS observations at 125 ± 50 km (Lellouch et al. 2014) at 60°S in 2009 July and at 80°S in 2007 November. For T53, we plot the methane mixing ratio retrieved with CIRS at 125 ± 50 km at the equator in 2007 December, and at 225 ± 50 km at 15°N in 2007 March and at 15°S in 2006 September. We also show the methane mixing ratio retrieved by the Gas Chromatograph and Mass Spectrometer (GC-MS; Niemann et al. 2010) and with the Descent Imager Spectral Radiometer (DISR; Bézard 2014; Rey et al. 2018), both on board Huygens, which landed in 2005 January at $\approx 10^\circ\text{S}$. The spatial resolutions of our vertical profiles are ± 6.25 km and ± 2.5 km for T10 and T53, respectively. In the right two panels, comparison between observed transmissions (red dots with error bars) and the model retrieval (blue dots) in the spectral range selected to retrieve the methane mixing ratio. The gap in spectra between 1.59 and 1.68 μm is due to uncorrected spectels in the VIMS instrument.

boundary (or impact factor) z_i of each layers, with $i = 1$ to N_D , as free parameters. The forward model is able to produce transmissions $T_m(z_i)$ at the impact factors z_i as a function of the haze properties (extinction $k_H(z_i)$ and spectral slope $\alpha_H(z_i)$) and the gas methane mixing ratio $X_{\text{CH}_4}(z_i)$, directly linked to the gas extinction ($k_{\text{CH}_4}(z_i)$). The model transmissions $T_m(z_i)$ are compared with the observed transmissions $T_o(z_i)$. To produce the retrieval, we use a Bayesian method along with a diffusive process to stabilize the algorithm. This is very suitable for this kind of triangular problems, that is, when the transmission at a given level only depends on the atmosphere properties above this level. It is also convenient because only Jacobians of the model are needed and the retrieval is performed with the iterative resolution of a matricial equation (see Appendices A and B for details). This method is very close to the one used by Maltagliati et al. (2015) and only the better methane linelist provided by Rey et al. (2018) brings a decisive improvement in our work.

3. Contrasted Stratospheric Methane Profiles

Figure 1 shows the retrieved vertical profiles for the two observations and the corresponding fits of the data. The methane profile at 70°S (T10) displays an enriched layer, with a mixing ratio up to $1.62\% \pm 0.10\%$ at 165 km, isolated in a relatively dry background atmosphere. Above this layer, the methane mixing ratio is quite constant with a value

$\approx 1.05\% \pm 0.10\%$. Below, it drops to $\approx 0.70\% \pm 0.20\%$ around 125 km. With the T53 observation, at 1°N , we find stratospheric values oscillating around 1.15% with error bars and amplitude both around 0.05% above 200 km and with a wavelength of $35_{-3,0}^{+4,5}$ km. Huygens found, near the equator, that methane decreases from 5% to 1.5% (Niemann et al. 2005, 2010) in the troposphere due to condensation. We then find that it further decreases to reach values around 1.0% to 1.15% in the mid-stratosphere at low latitudes instead of being constant as generally assumed. Our results are consistent with the effective values retrieved with CIRS in broad altitude ranges at 125 ± 50 km and 225 ± 50 km. However, our vertical resolutions allow us to be much more assertive and lift ambiguities about the mechanisms behind this methane distribution.

Figure 2 shows our results for the methane mixing ratios along with other values retrieved in the stratosphere and values evaluated at the cold trap (where the mixing ratio of air is capped due to the limitation by the saturation vapor pressure) from temperature measurements. Temperatures are stable with time in the low stratosphere (1 to 10 mbar) between 2005 and 2009 (Achterberg et al. 2011) and are expected to be even more stable at higher pressure (Lebonnois et al. 2012). We then consider temperatures gathered from data collected between 2005 and 2009, as a consistent set that depicts a steady state (Lellouch et al. 2014). On the other hand, post-equinoctial

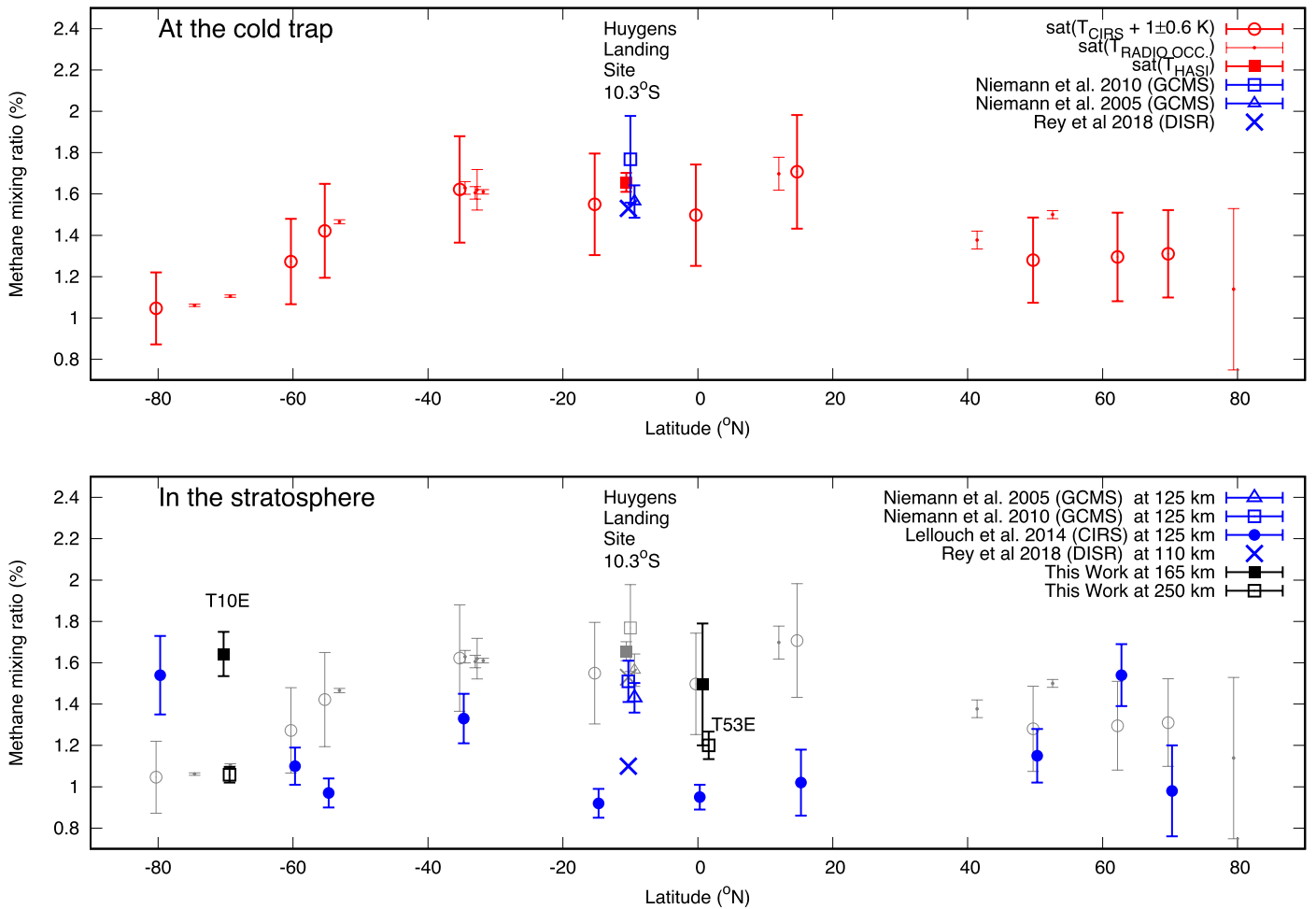


Figure 2. Top panel: methane mixing ratio as a function of the latitude at the cold trap (altitude ≈ 30 km). We show values measured with the GC–MS (Niemann et al. 2005, 2010) and retrieved with the DISR (updated values by Rey et al. 2018), both on board Huygens. We also show the saturation methane mixing ratio inferred from temperature measurements around the cold trap made by the Huygens Atmospheric Structure Instrument (HASI; Fulchignoni et al. 2005), from temperatures at 30 ± 1 km retrieved with the Radio Occultation Experiment (Schinder et al. 2011, 2012, 2020) and from temperatures retrieved by CIRS (Lellouch et al. 2014) around the cold trap. We only selected dates before the northern spring equinox. We add $+1 \pm 0.6$ K to CIRS temperatures in order to account for a systematic bias in retrieved temperatures at the cold trap, compared to HASI and to the radio-occultation temperature retrievals (Lellouch et al. 2014). This makes the saturation methane mixing ratios calculated from CIRS at the cold trap to be consistent with the “in situ” measurements made by Huygens. At the cold trap, methane condensate is expected to be pure ice (Tokano et al. 2006), then we use vapor pressures as published by Fray & Schmitt (2009). Bottom panel: methane mixing ratios retrieved in the stratosphere for this study along with the retrieval made by CIRS at 125 km and DISR at 110 km. The light gray symbols are those displayed in the top panel and reported here to facilitate comparisons.

changes are extremely rapid, even at the scale of a terrestrial year (e.g., Lebonnois et al. 2012; West et al. 2018; Teanby et al. 2019; Seignovert et al. 2021). Thus, we ignore in our discussion data taken after the equinox.

At first glance, the methane mixing ratios at 125 ± 50 km found by Lellouch et al. (2014) are highly variable with latitude. They appear unrelated to the latitudinal temperatures at the cold trap and the corresponding saturation mixing ratios, indicating a disconnection between the two fields (Figure 2). Near the equator (*T53*), the mixing ratio $1.25\% \pm 0.25\%$ around 150 km is also lower, yet consistent, compared to the value found by the Gas Chromatograph and Mass Spectrometer (GC–MS) at the cold trap. The value $1.15\% \pm 0.05\%$ around 250 km is much lower and not consistent with the value found at the cold trap or in the low stratosphere with the GC–MS. At 70°S (*T10*), the methane mixing ratio of $1.62\% \pm 0.10\%$ in the enriched layer at 165 km is much larger than the maximum value allowed by the cold trap temperature at 70°S , that is, $\approx 1.05\% \pm 0.19\%$. On the other hand, this value is comparable

to values allowed by the cold trap between tropics. There is no local source of methane in the atmosphere, and we do not expect that an eventual wave system could concentrate methane up to mixing ratios exceeding the background value by 50%. Such a layer is then a clear signature of an intrusion coming from a moist environment at another latitude. These results undermine the simple idea of a gaseous vertical flux through the tropopause at a global scale, locally limited by the saturation vapor pressure.

4. Methane Profiles Deciphered with Titan’s Circulation

To understand our results, we first discuss Titan’s circulation with the results of a global climate model (GCM) (Rannou et al. 2006). Although this is a two-dimensional (latitude–pressure) model, it accounts for the haze seasonal transport at a global scale up to the mesosphere, the cloud microphysics, and the radiative feedbacks. It predicts well the thick winter haze polarhood and the haze scavenging by clouds in the troposphere. The corresponding opacity fields are important drivers

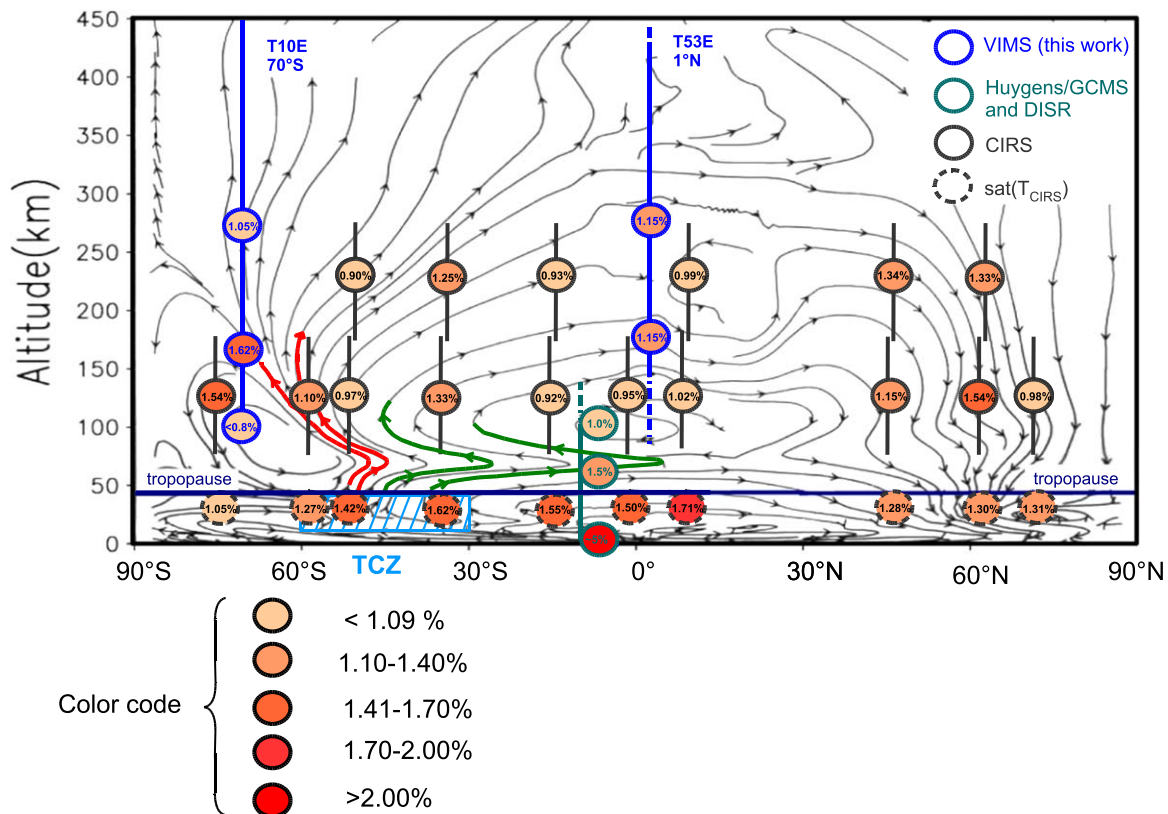


Figure 3. Circulation pattern averaged over one terrestrial year before the northern spring equinox as predicted by the Titan IPSL-GCM (Rannou et al. 2006) shown along with values of methane mixing ratios (values and color code) measured with Huygens (Niemann et al. 2010; Bézard 2014; Rey et al. 2018), with CIRS (Lellouch et al. 2014), and found in this work. Note, when comparing values, that CIRS values are averaged on broad vertical intervals of ± 50 km, while other values are local (less than ± 6.3 km). We also show the saturation mixing ratios for the cold trap temperature evaluated with CIRS (dashed circles). The mixing ratios shown here are reported, without their error bars, from Figure 2 except for the CIRS values at 225 km. In this case, error bars are between 0.15% and 0.47%. Two couples of wind streams are highlighted in red and green. They show how the methane-rich south tropical ascending branch at the TCZ, where convective clouds are frequently observed before equinox at latitude $45 \pm 15^\circ\text{S}$ (cyan hatched box; Rodriguez et al. 2011; Turtle et al. 2018), is connected to the methane-rich layer at 70°S and to the transition layer around 70 km in the equatorial region. High density of the stream lines is related to high mass flux. Therefore, the flux from the TCZ is quite constant and remains strong up to the edge of south polar region, while the branch toward the equator rapidly diverges and weakens. It should be kept in mind that the circulation fluctuates with time around average patterns, as those shown here.

of the circulation through the control of the solar flux at the surface and the cooling to space during the polar night (e.g., Rannou et al. 2004). To date, no existing 3D model accounts for all these couplings although they have major effects on the troposphere and low stratosphere circulation.

GCMs long predicted two opposite circulation cells below the stratosphere temperature inversion (Rannou et al. 2006) and a large thermally direct cell in the stratosphere with rapid post-equinoctial turnover (e.g., Rannou et al. 2004; Lebonnois et al. 2012; Larson et al. 2014; Lora et al. 2015; Figure 3). Before the northern spring equinox in 2009, at the time of T10 and T53, both troposphere cells have a lower branch near the surface that converges around 30°S – 40°S to give an ascending branch emerging from the troposphere (e.g., Rannou et al. 2006). This is equivalent to the tropospheric Hadley cells and the Inter-Tropical Convergence Zone (ITCZ) on Earth, except that cells extend up to the poles because of Titan’s slow rotation speed. Observation of the tropical clouds on Titan reveals the actual location of the Tropical Convergence Zone (TCZ) around $\simeq 45^\circ\text{S} \pm 15^\circ\text{S}$ (Rodriguez et al. 2011; Turtle et al. 2018). The prediction of clouds related to the Hadley-like cells in the coupled GCM (Rannou et al. 2006) at the location where they are actually observed validates this model for our discussion. However, it should be reminded that its results are also zonally and time averaged. The sporadic nature of the cloud events, the

short-term fluctuations, and longitude variabilities of the circulation are then erased.

At the TCZ, the ascending winds splits in two branches in the low stratosphere to close the Hadley-like cells. One cell drives air from the southern tropical tropopause to the south polar region up to around 150–200 km and sinks near the south pole. The other cell is forced to return equatorward almost horizontally at around 70 km altitude (upper branch) because the strong stratosphere temperature inversion, with high hydrostatic stability, prevents air from moving upward between tropics. This circulation leaves a strong dynamical signature with the zonal wind dropping due to the conservation of angular momentum. This dynamical signature is also observed at 70 km in reality, with zonal winds of 4 m s^{-1} in a thin layer of about 10 km thick, while layers above and below have zonal winds larger than 40 – 50 m s^{-1} (Bird et al. 2005). This specific layer makes a sharp transition between the Hadley-like cell and the stratosphere cell (Rannou et al. 2006; Lebonnois et al. 2012; Larson et al. 2014).

Methane mole fractions superimposed on the circulation pattern (Figure 3) show that the methane-rich layer observed during T10 is directly linked to an ascending branch that comes from the moist troposphere at the TCZ. It can convey methane to the south polar region up to about 160 km, above the cold and dry polar tropopause, and explains the intrusion layer. For

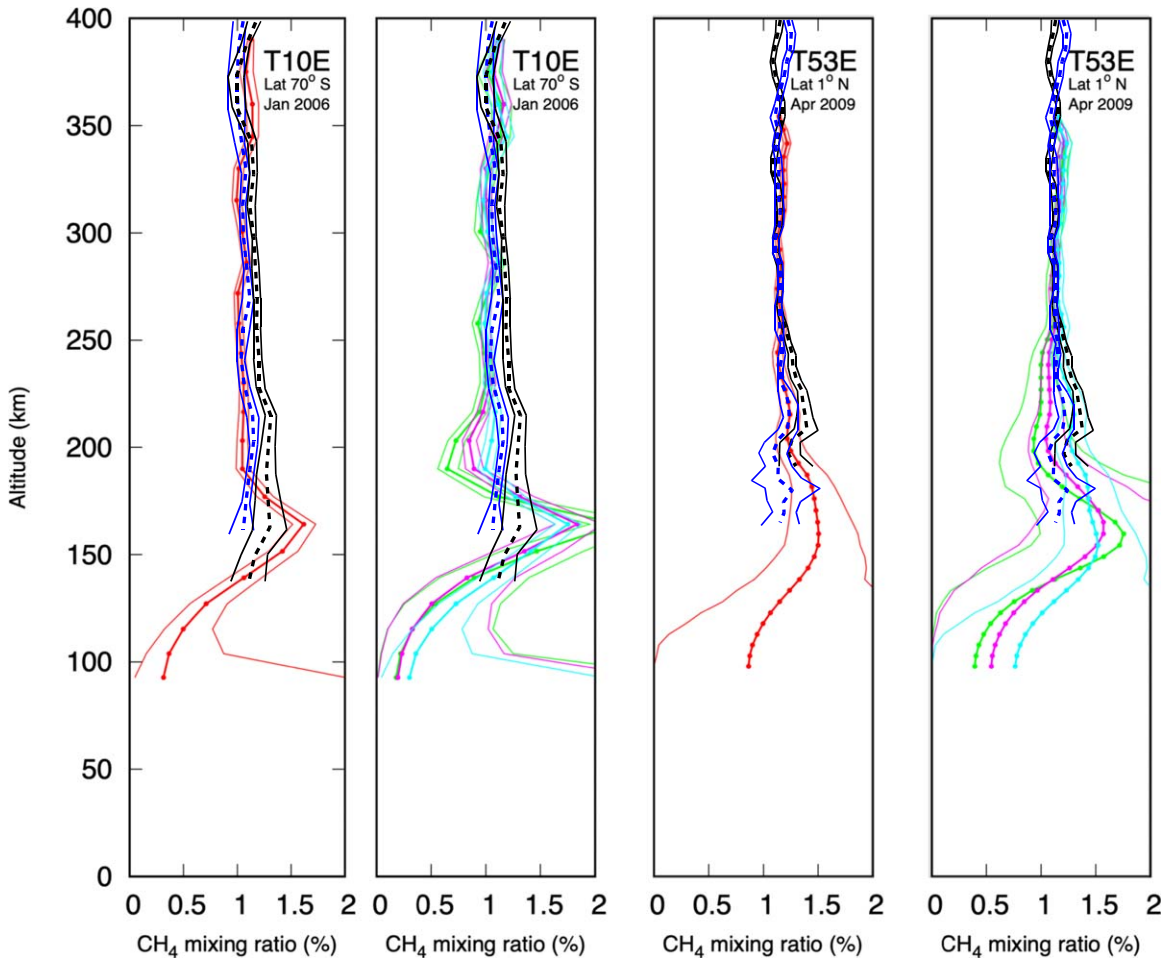


Figure 4. (First and third panels from the left) Methane mixing ratio (red dots) and the related error envelope (red curves) retrieved with the observation sets *T10* and *T53*, and with data at wavelengths between 0.88 and 2.03 μm shown along with the profiles retrieved by Maltagliati et al. (2015) with the 1.4 μm (dash black) and the 1.7 μm (dashed blue) methane bands. (Second and fourth panels from the left) Methane mixing ratios (color dots) and the related error envelopes (color curves) obtained with the observation sets *T10* and *T53*, and using the methane bands at 1.2 μm (light green), 1.4 μm (pink), and 1.7 μm (cyan), shown along with the profiles retrieved by Maltagliati et al. (2015) with the 1.4 μm (dash black) and the 1.7 μm (dashed blue) methane bands.

T53, we know that in the inter-tropical region, the transition in methane abundance from 1.5% to 1.15% (and $\simeq 1\%$ in Lellouch et al. 2014) takes place at the interface between the Hadley-like cell and the thermally direct stratosphere cell. The sharp drop in the zonal wind at the same altitude (Bird et al. 2005) associated with horizontal winds and to a strong temperature inversion indicates inhibited vertical exchanges. It marks the transition between a moist troposphere and low stratosphere, on one side, and the dryer background stratospheric air fed in methane through intrusions at some latitudes and not globally, on the other side. Clearly, the equatorial region is not one of these intrusion zones.

5. Humidification by Convection on Titan and on Earth

The dynamical origin of the stratospheric methane distribution is obvious in observations; however, GCMs accounting for nonconvective cloud microphysics and transport of species are not able to produce such distribution patterns (e.g., Rannou et al. 2006). Instead, they predict a constant methane mixing ratio in the stratosphere and the mesosphere that directly depends on the mixing ratio at the tropopause. This discrepancy underlines the role of cloud convection in transferring methane upward above the cold trap and into the stratosphere. Between 2004 and 2010, clouds are frequently observed at the TCZ

(Rodríguez et al. 2011; Turtle et al. 2018) and briefly near the equator during the equinoctial transition (Turtle et al. 2011). A photometric analysis shows that the core of these cloud systems can reach the high troposphere and the tropopause (Griffith et al. 2005). Mesoscale cloud models also show that with a surface humidity larger than 50% or 65%, convective clouds triggered by a perturbation in a moving air mass (Barth 2010) or in a static atmosphere easily reach high altitudes (Barth & Rafkin 2007, 2010). Large-scale ascending motions in the Hadley-like cells could trigger and facilitate convection. Convective clouds also inject methane ice particles, rather than vapor, without limitation due to the saturation vapor pressure at the cold trap. This would further enhance contrasts in the stratospheric methane distribution.

On Earth, by comparison, the entry of water vapor in the stratosphere between tropics and at midlatitudes is due to a slow gaseous advection, capped by cloud condensation, and also to overshooting of convective ice clouds in the lower stratosphere (e.g., Liu et al. 2010). Convective overshoots marginally account for several percent of the total flux of water, less than 18% according to the largest estimates (e.g., Dauhut et al. 2015; Ueyama et al. 2018). As a direct consequence, average water abundance in the tropical stratosphere is relatively homogenous and well related to the tropopause

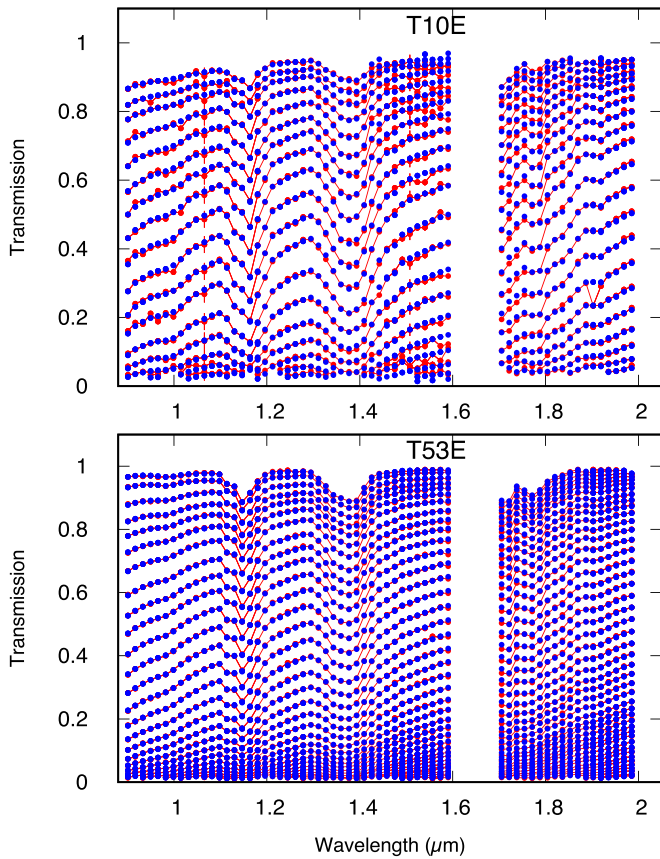


Figure 5. Comparison between observed transmissions (red dots with error bars) and the concatenation of the model retrieval (blue dots) made with the three methane bands separately. The gap in spectra between 1.59 and 1.68 μm is due to uncorrected spectels in the VIMS instrument.

temperature. Only oxidation of methane further produces inhomogeneities in the water stratospheric abundance. Earth’s case enlightens Titan’s case; on Earth, transport dominated by slow advection yields a quite uniform water mixing ratio in the stratosphere. On the contrary, on Titan, a substantial transfer by convection and an inhibited slow convection explains the sharp distribution in the stratosphere and a low background mixing ratio. In both atmospheric systems, slow advection and strong convective transports at the tropopause exist, but they do not have the same relative strengths. This difference in transports through the tropopause causes a different relationship between the tropospheric and stratospheric mixing ratio.

6. Consequence on Short- and Long-term Climate

After Huygens observations, the stratospheric methane abundance 1.4% is often used as a fiducial value to study other components of Titan (haze, clouds, temperature, other species, surface reflectivity, and thermal equilibrium). This is incorrect in two ways. First, the methane stratospheric abundance is around 1% to 1.1% on average rather than 1.4%. Second, its value is highly variable with space and probably with time. A simple test using the model of Coutelier et al. (2021) shows that a low methane abundance affects the retrieved haze opacity in stratosphere by $\simeq -4\%$ and the tropospheric mist opacity by $\simeq +7\%$. Although apparently moderate, these changes are about twice the accumulated errors produced by the instrumental uncertainties and the model bias on the retrieved values. Such a low methane abundance also

sets new conditions for the amount and the distribution of methane in the upper atmosphere (Yelle et al. 2021), with probable consequences on the escape rates and on the composition of aerosols and minor species.

More generally, humidification by convective entry and inhibition of slow vertical transfer also sets new conditions for the evaluation of the long-term climates of Titan (Lunine & Atreya 2008; Hayes et al. 2018). This way to regulate the stratosphere humidification strongly depends on the thermodynamical conditions behind cloud formation and convection, known to have onset and cutoff thresholds (e.g., Barth & Rafkin 2007, 2010; Barth 2010). Other climatic conditions, in the past or in the future, may radically change the way methane is transported upward due to convective motions. This would dim or enhance the flux of methane available for photochemistry much more and in a more complex way than anticipated with simple models based on slow advective transport (e.g., Lorenz et al. 1999). Of course, it would also change our perception of Titan’s history in shaking the exchange timescales and fluxes between the different methane reservoirs in Titan. Future progress in understanding the methane cycle on Titan will strongly rely on efficient and complete global climate models, associated with mesoscale models, able to treat the cloud microphysics and the moist convection process in detailed aspects.

Appendix A The Retrieval Model

Occultations probe extinction along lines of sight at the limb of the planet and are not sensitive to multiple scattering due to lower layers or to surface reflectivity. This kind of data easily allow us to separate methane and haze extinction since they extinct light in very different ways. To match the data, we divide the atmosphere according to the vertical sampling of observations and we compute the transmitted flux accounting for haze and gas extinction in each layer. We use data between 0.8 and 2.0 μm , where the signal is largely dominated by haze and methane extinction. Other methane bands, at 2.3 and 3.4 μm , are mixed with other undefined absorptions. This has been long remarked for the 3.4 μm fundamental band (e.g., Maltagliati et al. 2015), but, in this work, we also find a prominent unknown absorption that we discuss later. Methane absorption is given by the Rey et al. (2018) linelist and is treated with the correlated- k method (Goody et al. 1989) with 16 terms. Other gas properties are set with linelists published in the Hitran database (Gordon et al. 2017). The mixing ratio X_{CH_4} is the only free parameter relative to methane given for each layer. Haze extinction is computed with a model of scattering and absorption by fractal aggregates (Rannou et al. 1997), and the main characteristics of haze could be summarized as a vertical profile of extinction coefficient k_{H} at a reference wavelength, λ_0 , and the spectral slope $\alpha_{\text{H}} = \partial k_{\text{H}}(\lambda) / \partial \lambda$.

Appendix B Method Related to the Retrieval Procedure

To produce our analysis, we developed a retrieval model following the technique of the Bayesian inference (Rodgers 2000). Using the Bayes theorem, this technique allows for retrieving a parameter set x along with an estimated error σ_x from a set of observation y with observation errors σ_y . Each set

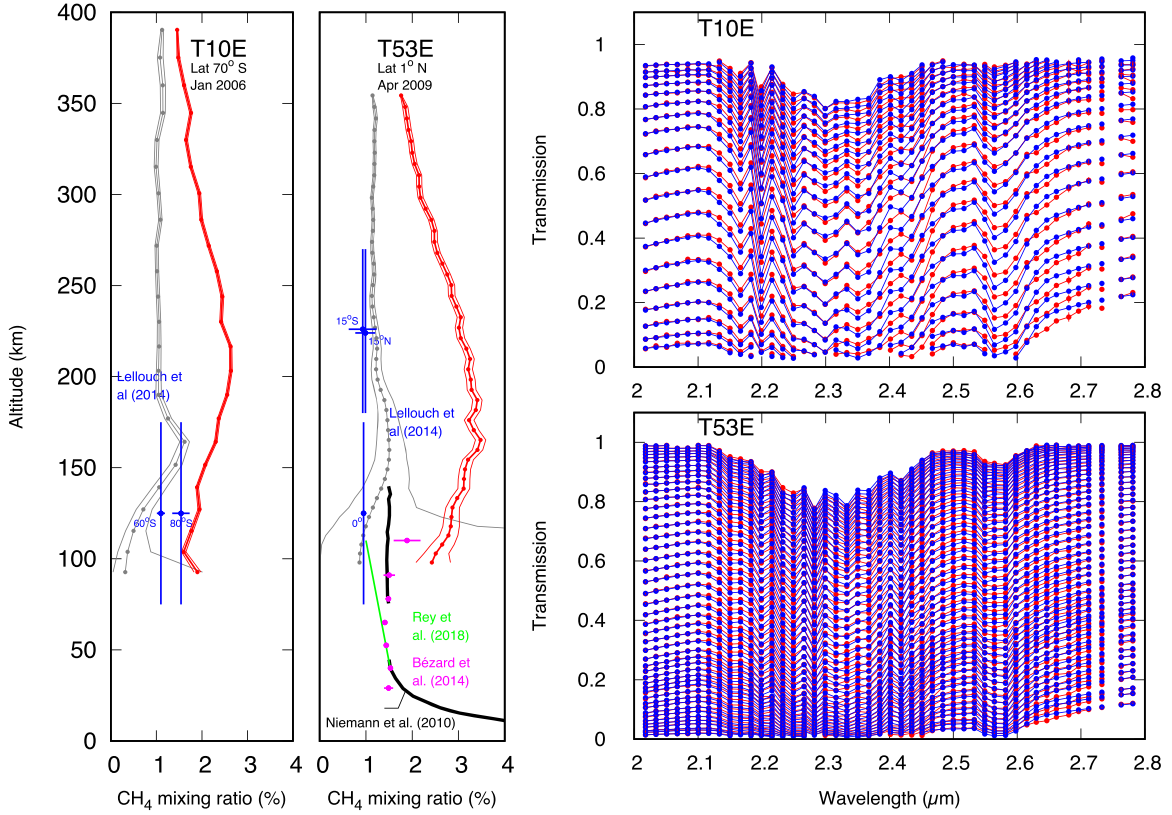


Figure 6. Left two panels: retrieved methane mixing ratio (red dots) and the related error envelope (red curves) with the observation sets T10 and T53, with wavelength between 2.03 and 2.8 μm . The gray profiles are those plotted in Figure 1 of the main text, with retrievals performed with parts of the spectra between 0.88 and 2 μm . We also plot methane mixing ratios from other works (Niemann et al. 2010; Bézard 2014; Lellouch et al. 2014; Rey et al. 2018). In the right two panels, comparison between observed transmissions (red dots with error bars) and the model retrieval (blue dots) in the spectral range selected to retrieve the methane mixing ratio. The gap in spectra corresponds to wavelengths where ethane is known to absorb, but cannot be modeled.

is represented by a vector. The strength of this approach essentially relies on the fact that we only need knowledge about the direct relationship between \mathbf{y} and \mathbf{x} . This relation is formally given by $\mathbf{y} = F(\mathbf{x})$, where F stands, in our case, for the radiative transfer model that links observed transmissions (\mathbf{y}) and the atmosphere parameters (\mathbf{x}) such as the haze extinction or gas mixing ratios.

To proceed, the function F has to be linearized around a given solution $\mathbf{y}(\mathbf{x}_0) = \mathbf{y}_0 + \partial F(\mathbf{x})/\partial \mathbf{x} \times (\mathbf{x} - \mathbf{x}_0)$, and where $\mathbf{y}_0 = F(\mathbf{x}_0)$. In this way, the set of partial derivatives $\partial F(\mathbf{x}_0)/\partial \mathbf{x}$ yields a matrix \mathbf{K} and the estimation for the best value of $\bar{\mathbf{x}}$ can be written as (Rogers 2000)

$$\bar{\mathbf{x}} = \mathbf{x}_0 + (\mathbf{K}^T \mathbf{S}_\epsilon^{-1} \mathbf{K})^{-1} \mathbf{K}^T \mathbf{S}_\epsilon^{-1} (\mathbf{y} - \mathbf{y}(\mathbf{x}_0)), \quad (1)$$

where \mathbf{S}_ϵ is the diagonal error matrix ($S_{\epsilon,(ij)} = \delta_{i,j}/\sigma_{y_i}^2$), $\mathbf{S} = (\mathbf{K}^T \mathbf{S}_\epsilon^{-1} \mathbf{K})^{-1}$ is the covariance matrix, and \mathbf{y} is the observation vector. If \mathbf{x}_0 is far from the best solution, the first estimated value $\bar{\mathbf{x}}$ will not be the best possible solution, but will be better than \mathbf{x}_0 . So we can start an iterative process to converge toward a solution that will be the most likely solution. In general, 20 to 40 iterations are needed to obtain an acceptable solution. It depends on the size of the vector \mathbf{x} . Notably, although we start with an initial guess for \mathbf{x}_0 , we do not include any a priori value in the retrieval matrix. The error on the retrieved parameter \mathbf{x} is given by the square root of the diagonal terms in the covariance matrix $\sigma_{x_i} = \sqrt{S_{ii}}$.

In order to avoid instabilities in the converged solution, we used a Tikhonov regularization. This consists of adding a

process analogous to a diffusion in the \mathbf{x} space to attenuate spurious oscillations. It takes the form of a matrix, \mathbf{H} , inserted in the covariance matrix as

$$\mathbf{S}^\dagger = (\mathbf{K}^T \mathbf{S}_\epsilon^{-1} \mathbf{K} + \beta \mathbf{H})^{-1} = (\mathbf{S}^{-1} + \beta \mathbf{H})^{-1}, \quad (2)$$

where \mathbf{H} is defined from the second-order derivative matrix \mathbf{L} as $\mathbf{H} = \mathbf{L}^2$ (e.g., Quémerais et al. 2006; Koskinen et al. 2011) and β is analogous to a diffusion coefficient. The order of magnitude of the matrix terms in \mathbf{L} is around $(\Delta Z)^{-2}$, with ΔZ the vertical distance between two consecutive observations. Setting β is a matter of tuning since there is no related physical process behind it. We scale β against the larger term of \mathbf{S}^{-1} , and we define a free factor γ so that we have $\beta = \gamma \Delta Z^4 \times \max(S_{i,j}^{-1})$. We tested several values of γ around 1 in order to remove small-scale oscillations but keeping the variations comparable to the atmosphere scale height ($\simeq 40$ km). We found that $\gamma \simeq 0.316$ gives the requested effect for retrieval performed with VIMS data at wavelengths shorter than 3 μm .

To retrieve haze and methane, we proceed in two steps. We first use the methane windows where haze extinction alone acts on transmission. This allows us to fix the haze vertical and spectral extinction. With this information about the haze layer, we then retrieve the vertical profile of the methane mixing ratio. We also need to account for the spectral shift of the VIMS instrument (e.g., Maltagliati et al. 2015) that we evaluated as part of the method. We use a subset of the data between 200 and 300 km, in the middle atmosphere, and we seek the best fit

with different values of the shift. With a cost function (χ^2) computed in the methane bands only, we are able to draw the value of χ^2 as a function of the wavelength shift. We then evaluate the best value of the shift and the error bars. Wavelength shifts for VIMS channels giving the best matches of data are $2.64^{+0.16}_{-0.21}$ nm for T10 and $9.40^{+0.10}_{-0.09}$ nm for T53. This significantly differs from RC19⁴ prescriptions.

Appendix C

Retrieval with Wavelengths Shorter than 2 μm

We show here comparisons between our results and results from the previous analysis (Maltagliati et al. 2015) obtained with the same data set. Figure 4 shows the retrieved vertical profiles of the methane mixing ratio for the two observations T10 and T53 as retrieved in this work and as retrieved by Maltagliati et al. (2015) in the bands at 1.4 and 1.7 μm . We also display the retrieval that we can perform with the three bands at 1.2, 1.4, and 1.7 μm separately. This shows that results concerning the methane mixing ratio differ from the one made by Maltagliati et al. (2015), especially concerning the enriched layer at 165 km for T10 that was not retrieved in the previous analysis. This feature is real since it appears separately in the three methane bands, in our analysis, with about the same contrast relative to the background. The background itself is also consistently found with the three different bands separately. The main difference between our work and the work by Maltagliati et al. (2015) is due to the high quality of the methane linelist that we use (e.g., Rey et al. 2018). The corresponding fits of the data are shown in Figure 5.

Appendix D

Retrieval in the 2.3 μm Methane Band

Figure 6 shows the retrieved vertical profiles for the two observations T10 and T53, in the two wavelength intervals: between 2.0 and 2.8 μm (band at 2.3 μm) and 0.88 to 2 μm . The modeled and retrieved spectra for the 2.3 μm band are also shown. In our results, we immediately remark that the 2.3 μm band cannot allow for a safe retrieval of the methane abundance because another species strongly interacts with methane absorption. This clearly appears in the spectra that cannot be a match with the same quality of fit as the spectra in between 0.88 and 2 μm (Figure 1 in the main text and Figure 5). Moreover, these poor fits are obtained with an excessive amount of methane. It was already well known that extra absorptions exist in the C–H fundamental band at 3.4 μm where methane does not absorb enough to explain observations (Bellucci et al. 2009; Maltagliati et al. 2015). Here, we clearly see that there is also an undefined absorption in the 2.3 μm band. As suggested by Maltagliati et al. (2015), ethane could be the absorbing gas, although it would appear surprising that a trace gas could compete with methane in one of its bands. If ethane is not responsible for the extra absorption in the 2.3 μm band, it would mean that something is not yet understood in Titan’s atmosphere opacity. For now, we consider that retrieval

of methane with the 2.3 μm band is not reliable and is only shown here for demonstration.

ORCID iDs

P. Rannou  <https://orcid.org/0000-0003-0836-723X>

S. Lebonnois  <https://orcid.org/0000-0002-2390-8164>

References

- Achterberg, R., Gierasch, P., Conrath, B., Michael Flasar, F., & Nixon, C. 2011, *Icar*, 211, 686
- Barth, E., & Rafkin, S. 2007, *GeoRL*, 34, L03203
- Barth, E., & Rafkin, S. 2010, *Icar*, 206, 467
- Barth, E. L. 2010, *P&SS*, 58, 1740
- Bellucci, A., Sicardy, B., Drossart, P., et al. 2009, *Icar*, 201, 198
- Bézar, B. 2014, *Icar*, 242, 64
- Bird, M. K., Allison, M., Asmar, S. W., et al. 2005, *Natur*, 438, 800
- Coutelier, M., Cordier, D., Seignovert, B., et al. 2021, *Icar*, 364, 114464
- Dauhut, T., Chaboureaud, J.-P., Escobar, J., & Mascart, P. 2015, *AtSciL*, 16, 135
- Faulk, S., Lora, J., Mitchell, J., & Milly, P. 2020, *NatAs*, 4, 390
- Fray, N., & Schmitt, B. 2009, *P&SS*, 57, 2053
- Fulchignoni, M., Ferri, F., Angrilli, F., et al. 2005, *Natur*, 438, 785
- Goody, R., West, R., Chen, L., & Crisp, D. 1989, *JQSRT*, 42, 539
- Gordon, I., Rothman, L., Hill, C., et al. 2017, *JQSRT*, 203, 3
- Griffith, C. A., Penteado, P., Baines, K., et al. 2005, *Sci*, 310, 474
- Hayes, A., Lorenz, R., & Lunine, J. 2018, *NatGe*, 11, 306
- Koskinen, T. T., Yelle, R. V., Snowden, D. S., Lavvas, P., Sandel, B. R., Capalbo, F. J., Benilan, Y., & West, R. A. 2011, *Icar*, 216, 507
- Larson, E. J., Toon, O. B., & Friedson, A. J. 2014, *Icar*, 243, 400
- Lebonnois, S., Burgalat, J., Rannou, P., & Charnay, B. 2012, *Icar*, 218, 707
- Lellouch, E., Bézar, B., Flasar, F. M., et al. 2014, *Icar*, 231, 323
- Liu, X. M., Rivière, E. D., Maréchal, V., Durry, G., Hamdouni, A., Arteta, J., & Khaykin, S. 2010, *ACP*, 10, 8267
- Lora, J. M., & Ádámkóvics, M. 2017, *Icar*, 286, 270
- Lora, J. M., Lunine, J. I., & Russell, J. L. 2015, *Icar*, 250, 516
- Lorenz, R. D., McKay, C. P., & Lunine, J. I. 1999, *P&SS*, 47, 1503
- Lunine, J., & Atreya, S. 2008, *NatGe*, 1, 159
- Maltagliati, L., Bézar, B., Vinatier, S., et al. 2015, *Icar*, 248, 1
- Mastrogioseppe, M., Poggiali, V., Hayes, A., et al. 2014, *GeoRL*, 41, 1432
- Niemann, H., Atreya, S., Bauer, S., et al. 2005, *Natur*, 438, 779
- Niemann, H. B., Atreya, S. K., Demick, J. E., et al. 2010, *JGRE*, 115, E12006
- Quémerais, E., Bertaux, J.-L., Korabiev, O., et al. 2006, *JGRE*, 111, E09S04
- Rannou, P., Cabane, M., Botet, R., & Chassefière, E. 1997, *JGR*, 102, 10997
- Rannou, P., Hourdin, F., McKay, C., & Luz, D. 2004, *Icar*, 170, 443
- Rannou, P., Montmessin, F., Hourdin, F., & Lebonnois, S. 2006, *Sci*, 311, 201
- Rannou, P., Seignovert, B., Le Mouélic, S., et al. 2018, *P&SS*, 151, 109
- Rey, M., Nikitin, A., Bézar, B., et al. 2018, *Icar*, 303, 114
- Rodgers, C. D. 2000, *Inverse Methods for Atmospheric Sounding: Theory and Practice* (Singapore: World Scientific)
- Rodriguez, S., Le Mouélic, S., Rannou, P., et al. 2011, *Icar*, 216, 89
- Schinder, P., Flasar, F., Marouf, E., et al. 2012, *Icar*, 221, 1020
- Schinder, P. J., Flasar, F. M., Marouf, E. A., et al. 2011, *Icar*, 215, 460
- Schinder, P. J., Flasar, F. M., Marouf, E. A., et al. 2020, *Icar*, 345, 113720
- Seignovert, B., Rannou, P., West, R. A., & Vinatier, S. 2021, *ApJ*, 907, 36
- Teany, N., Sylvestre, M., Sharkey, J., Nixon, C., Vinatier, S., & Irwin, P. 2019, *GeoRL*, 46, 3079
- Tokano, T. 2014, *Icar*, 231, 1
- Tokano, T., McKay, C., Neubauer, F., et al. 2006, *Natur*, 442, 432
- Turtle, E., Perry, J., Hayes, A., et al. 2011, *Sci*, 331, 1414
- Turtle, E. P., Perry, J. E., Barbara, J. M., et al. 2018, *GeoRL*, 45, 5320
- Ueyama, R., Jensen, E. J., & Pfister, L. 2018, *JGRD*, 123, 7576
- West, R. A., Seignovert, B., Rannou, P., et al. 2018, *NatAs*, 2, 495
- Yelle, R. V., Koskinen, T., & Palmer, M. 2021, *Icar*, 368, 114587

⁴ https://pds-imaging.jpl.nasa.gov/data/cassini/cassini_orbiter/vims-calibration-files/clark-et-al_vims-radiometric-calibration-pds-2018-v2.0.pdf